
ONE MODEL TO UNITE THEM ALL: PERSONALIZED FEDERATED LEARNING OF MULTI-CONTRAST MRI SYNTHESIS

A PREPRINT

**Onat Dalmaz^{1,2}, Usama Mirza^{1,2}, Gökberk Elmas^{1,2}, Muzaffer Özbeý^{1,2}, Salman UH Dar^{1,2},
Emir Ceyani³, Salman Avestimehr³, Tolga Çukur^{1,2,4}**

¹ Dept. of Electrical and Electronics Engineering, Bilkent University, Ankara 06800, Turkey

² National Magnetic Resonance Research Center (UMRAM), Bilkent University, Ankara 06800, Turkey

³ Dept. of Electrical and Computer Engineering, University of Southern California, Los Angeles 90089, USA

⁴ Neuroscience Program, Bilkent University, Ankara 06800, Turkey

July 15, 2022

ABSTRACT

Learning-based MRI translation involves a synthesis model that maps a source-contrast onto a target-contrast image. Multi-institutional collaborations are key to training synthesis models across broad datasets, yet centralized training involves privacy risks. Federated learning (FL) is a collaboration framework that instead adopts decentralized training to avoid sharing imaging data and mitigate privacy concerns. However, FL-trained models can be impaired by the inherent heterogeneity in the distribution of imaging data. On the one hand, implicit shifts in image distribution are evident across sites, even for a common translation task with fixed source-target configuration. Conversely, explicit shifts arise within and across sites when diverse translation tasks with varying source-target configurations are prescribed. To improve reliability against domain shifts, here we introduce the first personalized FL method for MRI Synthesis (pFLSynth). pFLSynth is based on an adversarial model equipped with a mapper that produces latents specific to individual sites and source-target contrasts. It leverages novel personalization blocks that adaptively tune the statistics and weighting of feature maps across the generator based on these latents. To further promote site-specificity, partial model aggregation is employed over downstream layers of the generator while upstream layers are retained locally. As such, pFLSynth enables training of a unified synthesis model that can reliably generalize across multiple sites and translation tasks. Comprehensive experiments on multi-site datasets clearly demonstrate the enhanced performance of pFLSynth against prior federated methods in multi-contrast MRI synthesis.

Keywords federated learning, personalization, MRI, synthesis, image translation, heterogeneity

1 Introduction

MRI is a powerful modality that offers non-invasive assessment of anatomy, with diagnostic information accumulated over multiple tissue contrasts [1]. Yet, it suffers from prolonged scan times due to its limited signal-to-noise ratio (SNR) efficiency. Costs associated with multi-contrast MRI protocols can prohibit the acquisition of each desired contrast or repeat run of a heavily corrupted contrast during an exam [2]. Contrast translation is a promising solution to this problem wherein omitted or corrupted images in the protocol are synthesized from the smaller subset of acquired images [3]. Deep learning methods have made significant advances in this domain, paving the way for centrally-trained models to achieve leaps in synthesis performance [4, 5, 6, 7]. Unfortunately, training of generalizable models for medical imaging tasks characteristically involves large, diverse datasets that are difficult to curate at a central institution given patient privacy risks [8].

Federated learning (FL) is a powerful framework to address this major limitation based on decentralized model training across multiple institutions [9, 10, 11, 12, 13, 14]. In the FL framework, a server sporadically aggregates locally-trained models at each site to compute a shared global model [15, 16], and then broadcasts the global model onto each site for further training. Thus, a learning-based model can be built collaboratively on diverse datasets from multiple sites without explicit sharing of imaging data [17]. That said, the resultant models can be impaired by the heterogeneity in the data distribution naturally evident for multi-institutional datasets [18, 19]. Previous studies on FL-based medical imaging have introduced several prominent approaches to cope with data heterogeneity in segmentation [20, 21, 14, 22, 23, 24], classification [13, 25, 26], and reconstruction [27, 28, 29] tasks. However, to our knowledge, no prior study has attempted to address data heterogeneity in FL-based MRI synthesis.

Learning-based MRI synthesis aims to predict unavailable target-contrast images of an anatomy provided as input acquired source-contrast images [30, 31, 32]. Synthesis models are trained based on datasets comprising paired or unpaired samples from the desired source-target configuration [7]. In a restricted setup, a multi-site model can be built for a single synthesis task with fixed source-target configuration (e.g., $T_1 \rightarrow T_2$ mapping at all sites where *source* \rightarrow *target*). Even in this limited setup, there will be implicit heterogeneity in the data distribution across sites due to reasonable variations in sequence parameters or imaging hardware [27, 29]. In a more flexible and realistic setup, a multi-site model can be built for multiple synthesis tasks resulting in variable source-target configurations prescribed within (e.g., $T_1 \rightarrow T_2$ and $T_2 \rightarrow T_1$ in all sites) or across sites (e.g., $T_1 \rightarrow T_2$ in some sites, $T_1 \rightarrow PD$ in others). In this case, there will be more explicit heterogeneity due to differences in the source- and target-contrast distributions. Unless adequately addressed, both implicit and explicit heterogeneity can induce notable performance losses in FL-based synthesis models.

Here, we introduce a novel method for personalized federated learning of multi-contrast MRI Synthesis (pFLSynth). Unlike previous methods, we propose a unified synthesis model that effectively addresses both implicit and explicit data heterogeneity in multi-institutional datasets. pFLSynth is based on an adversarial architecture whose generator comprises a residual bottleneck to distill task-critical information and a mapper that produces latent variables specific to individual sites and source-target contrasts. To cope with data heterogeneity, novel personalization blocks are introduced that adaptively tune the statistics and weighting of the feature maps across the generator based on the site- and contrast-specific latents. The residual bottleneck serves to derive a high-level semantic representation of source-contrast images. To promote a common representational space across sites, we propose partial model aggregation on downstream generator layers, while upstream layers are retained locally. Taken together, these elements render pFLSynth a unified synthesis model that can reliably generalize across multiple sites and synthesis tasks, preventing the need for training separate models for each site or each desired task. Comprehensive experiments on multi-institutional MRI datasets clearly demonstrate the superior performance of pFLSynth against prior federated models. Code for pFLSynth will be available at: <https://github.com/icon-lab/pFLSynth>.

Contributions

- We introduce the first FL method for personalized MRI synthesis to improve performance and flexibility in multi-site collaborations.
- To perform diverse synthesis tasks in separate sites with a unified model, our personalized architecture adapts the statistics and weighting of feature maps to each site and source-target configuration.
- We propose partial network aggregation on downstream layers to maintain site-general representations, and local upstream layers to maintain site-specific representations of MR images.

2 Related Work

In recent years, multi-contrast MRI synthesis has witnessed a surge in adoption of deep learning methods paralleling their success in other synthesis tasks [33, 34, 35, 36]. For translation of source-contrast onto target-contrast MR images, earlier studies in this domain proposed convolutional neural networks (CNN) coupled with pixel-wise loss terms [4, 5, 6]. To improve capture of tissue details and realism of synthetic images, generative adversarial networks (GAN) have also been proposed based on adversarial loss terms that indirectly learn the distribution of target-contrast images [7, 37, 38, 39, 40]. Regardless of the architecture, a common approach has been to aim for maximal performance by training a singular network model for each source-target configuration [41]. To mitigate the computational burden of building separate models, later studies have instead proposed unified models capable of performing multiple synthesis tasks in a single architecture [42, 43, 44, 45, 46]. However, despite the immense success demonstrated in learning-based MRI synthesis, prior studies have predominantly reported centralized training procedures that require cross-site transfer of imaging data [8].

To remedy privacy concerns related to data transfer, FL promotes decentralized training procedures that instead communicate model parameters across institutions [17]. This inherently distributes costs related to storage and modeling of data across sites [8]. Given their potential for multi-site collaborations, FL methods have readily been reported for several pervasive imaging tasks including segmentation [10, 9, 20, 14], classification [21, 12, 25, 26], reconstruction [27, 29, 28, 47], and image generation [48]. Yet, the potential of FL in multi-modal medical image translation remains largely unexplored. A recent study has proposed an FL method for multi-contrast MRI synthesis based on cycle-consistent GAN models [49]. Singular models were built independently for each separate source-target configuration. Promising results were reported for an FL setup where multiple sites were emulated by splitting of samples from individual public datasets. That said, no prior FL study has attempted to address the native data heterogeneity in multi-site datasets that can impair performance, or the limitation of singular models that can induce substantial computational burden in multi-institutional collaborations.

Here, we propose the first FL method for personalized image synthesis that addresses data heterogeneity in multi-site MRI datasets, and the first FL method for a unified synthesis model that performs multi-tasking under variable source-target configurations (Fig. 1). To enable these technical advances, pFLSynth introduces novel personalization blocks in the generator of an adversarial model with residual backbone (Fig. 2). Receiving site- and contrast-specific latent variables produced by a mapper, these blocks adaptively tune the statistics of feature maps via adaptive instance normalization [50], and tune the attributed importance of feature channels via channel weighting. Several recent studies have considered adaptive normalization for imaging tasks [51, 52, 47, 53, 54]. In [51], normalization used in a beamformer architecture for ultrasound imaging to switch among various output types. In [52, 47, 53], normalization was used to switch between the forward and backward mapping directions of a cycle-consistent architecture to lower model complexity. In [54], normalization was used to synthesize images at intermediate echo times (TE) via a centralized model trained on a dataset with

densely sampled TE values. Unlike prior studies, here we employ normalization layers in order to personalize a federated model for each individual site and source-target configuration, and couple them with novel channel weighting layers for improved specificity.

The proposed method employs shared generators and unshared discriminators across sites to improve reliability against information leaks as inspired by recent FL methods for adversarial architectures [55, 56]. Yet, instead of a global generator whose layers are shared to full extent among sites, pFLSynth adopts partial network aggregation where the generator is split centrally in its residual bottleneck to enable partial sharing. A recent study on MRI reconstruction has proposed sharing the encoder in a UNet backbone while keeping the decoder unshared [28], reporting that this may enhance site-specificity in the decoder segment of the reconstruction model. In contrast, here we propose to share the downstream layers of the residual generator while keeping upstream layers local to maintain specificity in the encoded representations. Taken together, these unique aspects enable pFLSynth to effectively address implicit and explicit heterogeneity in multi-contrast data for reliable MRI synthesis within and across sites.

3 Theory

3.1 MRI Synthesis with Adversarial Models

Adversarial models have emerged as a gold standard for multi-contrast MRI synthesis in recent years due to their exceptional sensitivity to high-frequency features [7, 57, 43, 58]. GANs perform adversarial learning via generator (G) and discriminator (D) subnetworks [7]. The generator predicts a synthetic target-contrast image (\hat{x}_t) given as input an actual source-contrast image (x_s), whereas the discriminator distinguishes actual (x_t) and synthetic target-contrast images. Assuming spatially-registered source and target images, a GAN is typically trained to minimize a compound objective with adversarial and pixel-wise loss terms:

$$\begin{aligned} \mathcal{L}_{syn}(\mathcal{D}, \theta) = & \mathbb{E}_{x_s, x_t} [-(D(x_t) - 1)^2 - D(G(x_s))^2 \\ & + \lambda_{pix} \|x_t - G(x_s)\|_1], \end{aligned} \quad (1)$$

where \mathbb{E} denotes expectation, \mathcal{D} are training data containing source and target images, $\theta = \{\theta_G, \theta_D\}$ are model parameters, the first two terms reflect the adversarial loss, the last term reflects the pixel-wise loss, and λ_{pix} is the relative weighing term for the pixel-wise loss. The traditional learning approach is based on centralized training, where data samples from multiple institutions are aggregated in a single repository [8]. This, however, introduces privacy risks for patients.

Alternatively, decentralized training can be performed via communication between a server and local sites [49]. The FL server hosts a global generator (G with parameters θ_G), while each site keeps a local copy (G^k for site k , where $k \in \{1, \dots, K\}$). Discriminators are typically unshared across sites to minimize the risk of information leak [55]. In each communication round, local copies are initialized with the global model transmitted by the server ($\theta_G^k \leftarrow \theta_G$). The local models are further trained to minimize a local synthesis loss:

$$(\theta_G^k, \theta_D^k) = \operatorname{argmin}_{\theta^k} \mathcal{L}_{syn}^k(\mathcal{D}^k, \theta^k), \quad (2)$$

where \mathcal{D}^k are local training data ($(x_{s_c}^k, x_{t_c}^k)$), and (s_c, t_c) denotes the c^{th} source-target configuration at site k ($c \in \{1, \dots, C\}$). After each round, locally trained models are aggregated on the server [15]:

$$\theta_G = \sum_{k=1}^K \alpha^k \theta_G^k, \quad (3)$$

where α^k denotes the relative site weights typically set to $\frac{n^k}{n}$, where n is the total number of training samples and n^k is the number of training samples at site k . The trained global model (G_{θ^*}) is

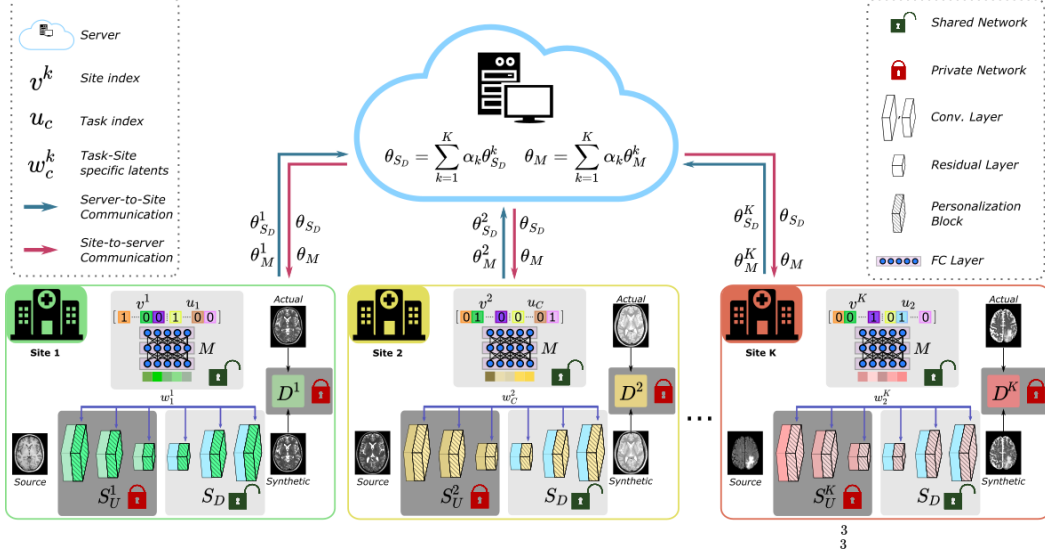


Figure 1: pFLSynth is a federated learning model for personalized MRI synthesis. The proposed architecture contains a mapper to produce site- and task-specific latents. These latents modulate feature maps via novel personalization blocks (PB) inserted across the generator. Partial network aggregation is adopted with shared downstream albeit unshared upstream layers to further promote personalization. These design elements enable pFLSynth to offer robust performance under data heterogeneity within- and across-sites.

eventually used for inference on each local site:

$$\hat{x}_{t_c}^k = G^*(x_{s_c}^k). \quad (4)$$

Native domain shifts exist between locally trained generators given implicit heterogeneity in data across sites (e.g., due to different scanners), as well as explicit heterogeneity due to variable source-target configurations within and across sites (i.e., different synthesis tasks). These domain shifts will cause the federated averaging to converge on a compromise model among various sites and synthesis tasks. As such, the resultant generator will perform suboptimally.

3.2 Personalized Federated Learning of MRI Synthesis

For improved generalization and flexibility in multi-site studies, we propose a personalized FL method for MRI synthesis, pFLSynth (Fig. 1). pFLSynth leverages novel personalization blocks (PB) composed of Adaptive Instance Normalization (AdaIN) [50] and novel Adaptive Channel Weighting (AdaCW) layers. Furthermore, partial network aggregation is adopted to further improve site-specificity, as well as communication efficiency and privacy. In the remainder of this section, we detail the network architecture and federated training procedures for pFLSynth.

3.2.1 Personalized Model Architecture

pFLSynth is a conditional adversarial model that receives a source image along with site and source-target configuration information as input. The generator employs a mapper that produces latent variables w for modulating feature maps, and a synthesizer to translate the source to the target image.

Mapper (M): M is an L_M -layer multi-layer perceptron (MLP) with leaky ReLU activation between fully-connected (FC) layers. Receiving the concatenation of binary indices for site identity ($v^k \in \mathbb{Z}_2^K$,

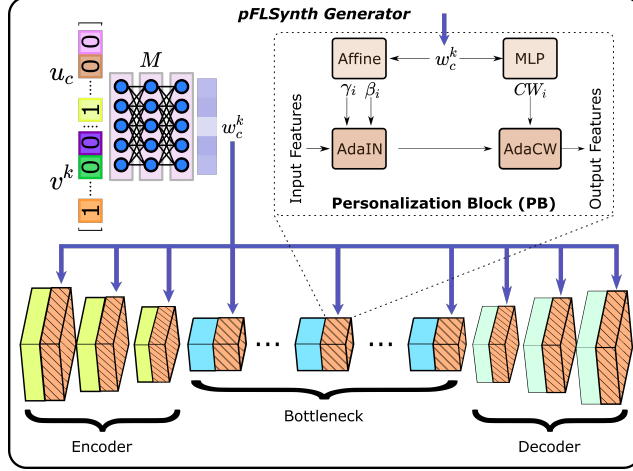


Figure 2: pFLSynth’s generator comprises a fully-connected mapper and a convolutional synthesizer (i.e., encoder-bottleneck-decoder). The mapper produces site- and task-specific latents w_c^k , given indices for site identity v^k and source-target configuration u_c . The synthesizer computes intermediate feature maps to translate between source and target images. A personalization block (PB) is inserted following each convolutional block that receives w_c^k . Each PB adaptively modulates feature maps to alter the statistics via AdaIN and channel weights via AdaCW layers.

$\mathbb{Z}_2 = \{0, 1\}$) and source-target configuration ($u_c \in \mathbb{Z}_2^C$), it produces a latent vector $w_c^k \in \mathbb{R}^J$ (see Fig. 2):

$$w_c^k = M(v^k \oplus u_c) \quad (5)$$

where \oplus denotes concatenation, J is the latent dimensionality. Parametrized as θ_M , M produces site- and task-specific latents to drive the personalization blocks in the synthesizer.

Synthesizer (S): Receiving as input a source image x_s and latent vector w_c^k , S generates a target image \hat{x}_t . The backbone is inspired by the ResNet model [7, 59] with a residual bottleneck between an encoder and a decoder (see Fig. 2). For each site and each source-target configuration, feature maps across the synthesizer can elicit divergent feature map statistics across the spatial and channel dimensions [60]. In turn, this divergence can compromise learning behavior. To mitigate heterogeneity in feature map statistics, here we introduce novel personalization blocks (PB) across the synthesizer. A PB is inserted after each convolutional layer in the encoder/decoder, and each residual block in the bottleneck. Let $S_L = \{S_{L_1}, S_{L_2}, \dots, S_{L_S}\}$ with parameters θ_{S_L} be the set of synthesizer stages. At the i th stage in S , input feature maps $f_{i-1} \in \mathbb{R}^{F_{i-1}, H_{i-1}, W_{i-1}}$ are processed via S_{L_i} :

$$g_i = S_{L_i}(f_{i-1}) \in \mathbb{R}^{F_i, H_i, W_i} \quad (6)$$

where F_i , H_i , and W_i are the number of channels, height, and width of the output map g_i . Next, g_i is processed in the i th personalization block PB_i .

To spatially modulate feature maps, PB_i transforms w_c^k into scale and bias vectors $\gamma_i, \beta_i \in \mathbb{R}^{F_i}$:

$$\gamma_i(k, c) = Q_i^\gamma w_c^k + b_i^\gamma; \beta_i(k, c) = Q_i^\beta w_c^k + b_i^\beta \quad (7)$$

where $Q_i^{\gamma, \beta} \in \mathbb{R}^{F_i, J}$ and $b_i^{\gamma, \beta} \in \mathbb{R}^{F_i}$ are learnable affine projections. An adaptive instance normalization (AdaIN) layer is then used to modulate the statistics of each channel [61, 50]:

$$g_i' = \text{AdaIN}(g_i, \gamma_i, \beta_i) = \begin{bmatrix} \gamma_i[1] \frac{g_i[1] - \mu(g_i[1])\mathbf{1}}{\sigma(g_i[1])} + \beta_i[1]\mathbf{1} \\ \gamma_i[2] \frac{g_i[2] - \mu(g_i[2])\mathbf{1}}{\sigma(g_i[2])} + \beta_i[2]\mathbf{1} \\ \vdots \end{bmatrix} \quad (8)$$

where $\mathbf{1} \in \mathbb{R}^{H_j, W_j}$ is a matrix of ones, μ, σ compute the mean and standard deviation of individual channels $g_i[j] \in \mathbb{R}^{H_i, W_i}$.

Next, a novel adaptive channel weighting (AdaCW) layer is used that weights feature channels according to their task relevance. The latent vector w is transformed via an L_{CW} -layered MLP with sigmoid activation in the last layer to range the output in $[0, 1]$:

$$CW_i(k, c) = \text{MLP}(w_c^k), \quad (9)$$

where $CW_i \in \mathbb{R}^{F_i}$ is the relevance vector across channels. Feature maps from the AdaIN layer are then modulated:

$$f_{i+1} = \text{AdaCW}(g_i, CW_i) = \begin{bmatrix} g_i[1] \odot CW_i[1]\mathbf{1} \\ g_i[2] \odot CW_i[2]\mathbf{1} \\ \vdots \end{bmatrix} \quad (10)$$

where \odot denotes Hadamard product, and f_{i+1} is the output feature map. The overall mapping through S is a cascade of projections through convolutional layers and PBs:

$$\hat{x}_t = S_{L_S} \circ PB_{L_S-1} \circ S_{L_S-1} \circ \cdots \circ PB_1 \circ S_1(x_s, w_c^k) \quad (11)$$

where \circ denotes functional composition.

Partial Network Aggregation: S is split at stage L_U into two disjoint subsets $S_U = \{S_{L_1}, S_{L_2}, \dots, S_{L_U}\}$ and $S_D = \{S_{L_U+1}, S_{L_U+2}, \dots, S_{L_S}\}$ where $L_U \in \{1, 2, \dots, L_S\}$. The set of upstream stages S_U with parameters $\theta_{S_U}^k, k \in \{1, 2, \dots, N_k\}$ are kept locally at each site. In contrast, the set of downstream stages S_D with parameters θ_{S_D} commonly across sites are communicated to the server. Thus, instead of aggregating the entire synthesizer, pFLsynth only aggregates downstream layers. This partial aggregation improves site-specificity in the encoded representations of the source images.

Discriminator (D): Unshared discriminators are used across sites to improve privacy preservation. Accordingly, a local discriminator D^k with parameters θ_D^k is trained at site k based on a conditional patch-based architecture [7]. Conditioned on the source image, D^k estimates the probability that x is drawn from the distribution of actual target images:

$$p_D = D(x|x_s), \quad (12)$$

where x can be an actual or synthetic target image, and p_D is the output.

3.2.2 Federated Training

To train pFLSynth, decentralized learning is performed for a total of P communication rounds between the FL server and individual sites (see Fig. 1, Alg. 1). The downstream synthesizer and mapper are shared across sites, albeit the upstream synthesizer and discriminator are unshared. In the first round, the server randomly initializes a global generator $G = \{S, M\}$ with parameters θ_G . At

the start of each round, the server broadcasts the global downstream synthesizer S_D and the global mapper M for the sites to update their local copies:

$$\theta_{S_D}^k \leftarrow \theta_{S_D}; \theta_M^k \leftarrow \theta_M; k = 1, 2, \dots, K \quad (13)$$

The local upstream synthesizer and discriminator are instead initialized with their local states from the previous round:

$$\theta_{S_U}^k \leftarrow \theta_{S_U}^k; \theta_D^k \leftarrow \theta_D^k, \quad (14)$$

A local generator is formed by combining synthesizer components with the mapper:

$$G^k = \{(S_U^k \sqcup S_D^k), M^k\} \quad (15)$$

Next, each local generator is trained for E epochs on the respective local dataset. Note that pFLSynth is a unified model that can consolidate different synthesis tasks within and across sites. Let \mathcal{D}^k be the training data for the source-target configurations at site k :

$$\mathcal{D}^k = \{(x_{s_1}^k, x_{t_1}^k), \dots, (x_{s_C}^k, x_{t_C}^k)\}, \quad (16)$$

where the number of configuration C is taken as fixed across sites without loss of generality. Local models are trained to minimize a compound local synthesis loss summed across tasks:

$$\begin{aligned} \mathcal{L}_{syn}^k(\mathcal{D}^k, \theta^k) = & \sum_{c=1}^C \mathbb{E}_{x_{s_c}^k, x_{t_c}^k} [-(D^k(x_{t_c}^k) - 1)^2 - D^k(G^k(x_{s_c}^k, v^k, u_c))^2 \\ & + \lambda_{pix} \|x_{t_c}^k - G^k(x_{s_c}^k, v^k, u_c)\|_1] \end{aligned} \quad (17)$$

At the end of a communication round, each site sends its downstream synthesizer and mapper to the server for aggregation into the global model [62]:

$$\theta_{S_D} = \sum_{k=1}^K \frac{n^k}{n} \theta_{S_D}^k; \theta_M = \sum_{k=1}^K \frac{n^k}{n} \theta_M^k \quad (18)$$

During inference, each site forms a personalized generator as in Eq. 15 to perform contrast translation:

$$\hat{x}_{t_c}^k = G^{k*}(x_{s_c}^k, v^k, u_c). \quad (19)$$

Because the federated generator performs adaptive mapping at each site and for each synthesis task, it achieves improved generalization performance.

4 Methods

4.1 Datasets

Experiments were conducted on four public datasets with multi-contrast brain MR images: IXI (<https://brain-development.org/ixi-dataset/>), BRATS [63], MIDAS [64], and OASIS [65]. IXI and MIDAS contain data from healthy subjects, BRATS contains data from glioma patients, and OASIS contains data from subjects with various levels of cognitive decline. Each dataset was treated as a separate site in the FL setup. Subjects in each dataset were split into non-overlapping training, validation, and test sets.

IXI: T₁-, T₂-, and Proton Density (PD)-weighted images from 53 subjects were analyzed with a (25,10,18) split for the training, validation and test sets. The training set contained 2780 cross-sections per source-target configuration. For each subject, T₂- and PD-weighted images were registered onto

Algorithm 1: Training of pFLSynth

Data: $\{\mathcal{D}^1, \dots, \mathcal{D}^K\}$ from K sites
Input: P : number of communication rounds
 E : number of local epochs
 G : global generator with params. $\theta_G = \{(S_U \sqcup S_D), M\}$
 G^1, \dots, G^K : local generators with $\theta_{G^1}, \dots, \theta_{G^K}$
 D^1, \dots, D^K : local discriminators with $\theta_{D^1}, \dots, \theta_{D^K}$
 $Opt()$: optimizer for parameter updates
 $FedAvg()$: federated averaging
Output: $\theta_{G^K}^*$ personalized generators

```

1 Randomly initialize  $\theta_G$  and  $\theta_{D^1}, \dots, \theta_{D^K}$ 
2 for  $p = 1$  to  $P$  do
3   for  $k = 1$  to  $K$  do
4      $\theta_{S_D}^k \leftarrow \theta_{S_D}$ ,  $\theta_M^k \leftarrow \theta_M$                                 // receive global subnetworks
5     for  $e = 1$  to  $E$  do
6       Calculate  $\nabla_{\theta_G^k} \mathcal{L}_{syn}^k(\mathcal{D}^k)$  based on Eq. 17
7        $\theta_G^k \leftarrow \theta_G^k - Opt(\nabla_{\theta_G^k} \mathcal{L}_{syn}^k(\mathcal{D}^k))$           // update local generators
8       Calculate  $\nabla_{\theta_D^k} \mathcal{L}_{syn}^k(\mathcal{D}^k)$  based on Eq. 17
9        $\theta_D^k \leftarrow \theta_D^k - Opt(\nabla_{\theta_D^k} \mathcal{L}_{syn}^k(\mathcal{D}^k))$           // update local discriminators
10     $\theta_{S_D} \leftarrow FedAvg(\theta_{S_D}^k)$ ,  $\theta_M \leftarrow FedAvg(\theta_M^k)$           // aggregate subnetworks

```

T_1 -weighted images via FSL using affine transformation based on mutual information [66]. For T_1 , a 3D MP-RAGE sequence, TE = 4.6ms, TR = 9.8ms, flip angle = 8° , spatial resolution = 0.94x0.94x1.2mm³ were prescribed. For T_2 , a 2D fast spin-echo sequence, TR = 8178ms, TE = 100ms, flip angle = 90° , spatial resolution = 0.94x0.94x1.2mm³ were prescribed. For PD, a 2D fast spin-echo sequence, TR = 8178ms, TE = 8ms, flip angle = 90° , spatial resolution = 0.94x0.94x1.2mm³ were prescribed.

BRATS: T_1 -, T_2 -, and T_2 -Fluid Attenuation Inversion Recovery (FLAIR)-weighted images from 55 subjects were analyzed with a (25,10,20) split. The training set contained 2500 cross-sections per source-target configuration. Scans were acquired under various settings without a common scan protocol. As publicly shared, MR images were at 1x1x1mm³ resolution, skull-stripped, and co-registered to the same anatomical template.

MIDAS: T_1 - and T_2 -weighted images from 66 subjects were analyzed with a (48,5,13) split. The training set contained 3874 cross-sections per source-target configuration. As publicly shared, MR images were co-registered to an anatomical template. For T_1 , a 3D gradient-echo sequence, TR=14ms, TE=7.7ms, flip angle = 25° , spatial resolution = 1x1x1mm³ were prescribed. For T_2 , a 2D spin-echo sequence, TR=7730ms, TE=80ms, flip angle = 90° , spatial resolution = 1x1x1mm³ were prescribed.

OASIS: T_1 -, T_2 -, and T_2 -FLAIR-weighted images from 48 subjects were analyzed with a (22,9,17) split. The training set contained 2780 cross-sections per source-target configuration. For each subject, T_2 - and FLAIR-weighted images were registered onto T_1 -weighted images via FSL using affine transformation based on mutual information [66]. For T_1 , a 3D MP-RAGE sequence, TE=4.0ms, TR=9.7ms, flip angle = 10° were prescribed. For T_2 , a 2D spin-echo sequence, TE=86ms, TR = 6150ms, flip angle = 120° were prescribed. For FLAIR, a 2D inversion-recovery sequence, TE=91ms, TR = 9000ms, flip angle = 150° were prescribed.

4.2 Competing Methods

We demonstrated pFLSynth against a centralized benchmark model [7], and federated baseline models [55, 67, 49, 47, 68]. For each competing method, hyperparameter selection was performed via identical cross-validation procedures. In all models, generators were shared across sites, but a separate local discriminator was used per site and per source-target configuration for improved performance.

Centralized: A non-federated synthesis model was considered [7]. The Central model had matching loss function and architecture to pFLSynth, albeit personalization components were removed (the mapper and personalization blocks). Centralized training was performed following data aggregation across sites. For improved performance, a separate discriminator was utilized while processing training data from each site and source-target configuration. The Central model serves as a privacy-violating benchmark for pFLSynth.

FedGAN: A federated synthesis model was implemented with matching loss function and architecture to pFLSynth, but without the mapper and PBs. In contrast to pFLSynth, FedGAN aggregated the entire generator on the server, so it serves as a non-personalized benchmark for pFLSynth.

FedMRI: A federated model originally proposed preserving site-specificity in MRI reconstruction was considered [67]. FedMRI was implemented based on a U-Net backbone, whose upstream layers were shared while downstream layers were kept site-specific as in [67]. A discriminator was added to adopt FedMRI for adversarial synthesis, and matching loss function to pFLSynth was used.

FedMM: The federated implementation of a unified MRI synthesis model (MM-GAN) was considered [68]. FedMM was implemented with a U-Net generator and multiple input-output channels to cope with different source-target configurations as described in [68]. The entire generator was aggregated on the server. For fair comparison, curriculum learning was omitted to ensure standard sample selection for all methods.

FedMed: A recent federated model for multi-contrast MRI synthesis was considered [49]. FedMed (abbreviated from FedMed-GAN) was implemented with a U-net generator, where the entire generator was aggregated on the server as in [49]. FedMed was originally proposed for unpaired synthesis based on cycle-consistency loss. Only the forward mapping generator was retained to adapt it for paired synthesis, and matching loss function to pFLSynth was used. For fair comparison, differential privacy procedures were omitted.

FedCycle: Originally proposed for low-dose CT denoising, FedCycle (abbreviated from FedCycleGAN) is a federated model based on a switchable backbone to reduce model complexity [47]. FedCycle was implemented with a U-Net generator and adaptive normalization blocks as in [47]. To adopt FedCycle for paired synthesis, only the forward mapping generator was retained, and matching loss function to pFLSynth was used. The switching mechanism was used to adapt the model to different source-target configurations as in pFLSynth.

4.3 Architectural Details

The pFLSynth model is composed of a mapper, a synthesizer, and a discriminator. The mapper contained $L_M = 6$ layers. The synthesizer followed an encoder-bottleneck-decoder structure with a total of $L_S = 15$ stages. The encoder contained three stages ($e1 - e3$), each with a convolutional layer followed by a PB, and kernel sizes were 7, 3, 3 across stages. The bottleneck contained nine PBs and nine residual layers ($r1 - r9$) with kernel size 3 [59]. The decoder contained two PBs and three convolutional layers ($d1 - d3$) of kernel sizes 3, 3, and 7. The encoder mapped source images to $\mathbb{R}^{256,64,64}$, the bottleneck retained dimensionality, and the decoder mapped feature maps from the

bottleneck to $\mathbb{R}^{1,256,256}$. The discriminator contained five convolutional layers of kernel size 4. An FL setup comprising $K = 4$ different datasets was considered. Accordingly, a binary site identity index of $v^k \in \mathbb{Z}_2^4$ was used. The datasets examined included 4 MRI contrasts, namely T_1 , T_2 , PD, and FLAIR. Thus, a source-target configuration index of $u_c \in \mathbb{Z}_2^8$ was formed by concatenating source and target identity. The mapper received these indices and produced a latent vector $w_c^k \in \mathbb{R}^{512}$. The MLP in AdaCW had 2 FC layers with 64 hidden neurons. The splitting layer in the synthesizer (L_U) was selected as $r5$ (i.e., midpoint of the bottleneck) based on validation performance, taken as peak signal-to-noise ratio (PSNR) for a representative $T_1 \rightarrow T_2$ task.

4.4 Modeling Procedures

For fair comparison, all competing models were trained using the same discriminator in Eq. 12 and compound synthesis loss in Eq. 17. Hyperparameter selection, including weighting of the pixel-wise loss term, number of communication rounds, number of epochs, and learning rate was performed via cross-validation. A common set of hyperparameters that yielded near-optimal results across models and datasets were selected. Accordingly, training was performed via the Adam optimizer with $\beta_1 = 0.5$ and $\beta_2 = 0.999$. For centralized models, training lasted 150 epochs. Training lasted $P=150$ rounds for federated models with $E=1$ local epochs each. Learning rate was set as 0.0002 during the initial 75 epochs and linearly decayed to 0 during the remaining epochs. The pixel-wise loss weight was set to $\lambda_{pix} = 100$. Models were implemented using the PyTorch framework and executed on Nvidia RTX 3090 GPUs.

Synthesis performance was evaluated via PSNR, Structural Similarity Index (SSIM), and Fretchet Inception Distance (FID) [69] metrics. PSNR and SSIM were measured between synthetic and reference target-contrast images. Results were reported as mean and standard deviation across a set of test subjects that did not overlap with the training or validation sets. Wilcoxon signed-rank tests were conducted to assess the significance of the performance differences among competing methods ($p<0.05$).

5 Results

5.1 Common task configuration within and across sites

In this study, federated learning experiments were conducted in a four-site setup based on IXI, BRATS, MIDAS, and OASIS datasets. We first demonstrated pFLSynth for decentralized modeling of a single synthesis task within each site, which was also common across sites (i.e., $T_1 \rightarrow T_2$). This common task configuration reflects the influence of implicit heterogeneity in the data distribution due to differences in scanners and protocols used to collect the same MRI contrasts across sites. Quantitative performance metrics for pFLSynth, state-of-the-art federated baselines and a centrally trained benchmark are listed in Table 1. pFLSynth outperforms all federated baselines at each site ($p<0.05$), and offers on par performance with the central benchmark. On average across sites, pFLSynth achieves 0.8dB higher PSNR, 1.4% higher SSIM, and 5.8 lower FID over competing federated baselines. Representative target images synthesized by competing methods are displayed in Fig. 3. pFLSynth generates images with reduced artifacts and noise, and it achieves the closest tissue depiction to the ground-truth target images. Notably, pFLSynth offers a more accurate depiction of pathological tissues. Taken together, these results indicate that pFLSynth maintains high image quality and generates target images that closely approximate the distribution of ground truth.

5.2 Variable task configuration within sites

Next, we demonstrated pFLSynth for simultaneous modeling of two synthesis tasks within each site, albeit the tasks were common across sites (i.e., $T_1 \rightarrow T_2$ and $T_2 \rightarrow T_1$). This variable task

		IXI	BRATS	MIDAS	OASIS
		$T_1 \rightarrow T_2$	$T_1 \rightarrow T_2$	$T_1 \rightarrow T_2$	$T_1 \rightarrow T_2$
Central	P \uparrow	28.6 \pm 1.3	26.1 \pm 0.9	28.1 \pm 0.5	25.2 \pm 0.6
	S \uparrow	94.3 \pm 1.3	93.0 \pm 1.1	91.9 \pm 0.9	83.7 \pm 2.4
	F \downarrow	7.4	24.8	9.7	18.1
pFLSynth	P \uparrow	28.6\pm1.3	26.3\pm1.0	28.2\pm0.5	25.1\pm0.6
	S \uparrow	94.4\pm1.4	93.3\pm1.1	92.1\pm0.8	84.4\pm2.0
	F \downarrow	7.7	23.9	9.2	30.2
FedGAN	P \uparrow	27.6 \pm 1.1	26.0 \pm 0.9	27.9 \pm 0.6	24.6 \pm 0.7
	S \uparrow	93.2 \pm 1.3	92.9 \pm 1.1	91.6 \pm 0.8	83.4 \pm 2.6
	F \downarrow	11.5	24.2	9.9	40.2
FedMRI	P \uparrow	27.9 \pm 1.2	25.7 \pm 0.8	27.7 \pm 0.5	23.8 \pm 0.8
	S \uparrow	93.7 \pm 1.3	92.9 \pm 1.1	91.2 \pm 1.0	82.7 \pm 2.1
	F \downarrow	9.6	32.5	11.3	43.0
FedMM	P \uparrow	26.9 \pm 1.1	25.6 \pm 0.8	27.9 \pm 0.6	24.3 \pm 0.5
	S \uparrow	91.7 \pm 1.9	92.6 \pm 1.1	91.5 \pm 0.9	80.0 \pm 2.4
	F \downarrow	18.1	28.3	9.5	42.3
FedMed	P \uparrow	27.1 \pm 1.1	25.6 \pm 0.7	27.8 \pm 0.6	24.3 \pm 0.5
	S \uparrow	92.5 \pm 1.4	92.5 \pm 1.1	91.3 \pm 0.8	81.0 \pm 1.9
	F \downarrow	13.0	26.6	9.4	47.0
FedCycle	P \uparrow	27.2 \pm 1.1	25.5 \pm 0.8	27.8 \pm 0.6	24.2 \pm 0.5
	S \uparrow	92.8 \pm 1.5	92.4 \pm 1.1	91.5 \pm 0.9	80.8 \pm 2.2
	F \downarrow	13.4	25.5	9.8	45.8

Table 1: Performance of federated models in a common task within and across sites (i.e., $T_1 \rightarrow T_2$). A centrally trained benchmark is also reported. PSNR (P, dB) and SSIM (S, %) are listed as mean \pm std across test subjects, whereas FID (F) summarizes the entire test set. Boldface indicates the top-performing federated model for each site, task, and metric.

configuration creates explicit heterogeneity in the distribution of source and target contrasts, which synthesis models have to cope with to maintain high fidelity. Performance metrics for competing methods are listed in Table 2. pFLSynth outperforms all federated baselines at each site ($p < 0.05$), except for BRATS, where FedGAN yields lower FID, and MIDAS, where FedCycle yields higher PSNR in $T_2 \rightarrow T_1$. Again, pFLSynth performs on par with the centralized case. On average across tasks and sites, pFLSynth achieves 0.9dB higher PSNR, 1.9% higher SSIM, and 7.4 lower FID over competing federated baselines. Representative target images synthesized by competing methods are displayed in Fig. 4. In contrast to competing methods, pFLSynth achieves lower artifacts and noise along with a more accurate depiction of pathological tissue. These results show that pFLSynth can reliably cope with explicit data heterogeneity that arises in multi-task learning within sites.

5.3 Variable task configuration within and across sites

Lastly, we demonstrated pFLSynth for simultaneous modeling of diverse synthesis tasks both within and across sites. Specifically, $T_2 \rightarrow T_1$ and $T_2 \rightarrow$ PD in IXI, $T_2 \rightarrow T_1$ and FR \rightarrow T_2 in BRATS, $T_1 \rightarrow T_2$ and $T_2 \rightarrow T_1$ in MIDAS, $T_2 \rightarrow T_1$ and $T_2 \rightarrow$ FR in OASIS were considered. This diverse task configuration creates a very high degree of heterogeneity, so it constitutes the stringent test among all examined configurations for all synthesis methods, including the central benchmark. Performance metrics are listed in Table 3. pFLSynth outperforms all federated baselines at each site ($p < 0.05$), except for MIDAS, where FedCycle yields higher PSNR and FedGAN yields higher SSIM, and

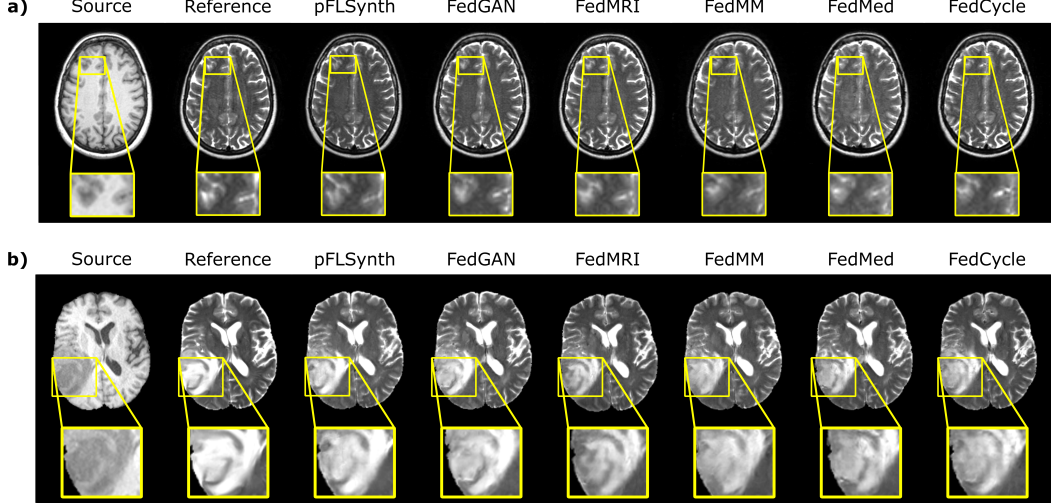


Figure 3: Federated synthesis under a common task configuration within and across sites, $T_1 \rightarrow T_2$. Source, reference target, and synthetic target images from competing methods are shown. Representative images are shown from a) IXI, b) BRATS. Overall, pFLSynth synthesizes images with fewer artifacts and lower noise levels compared to other federated methods.

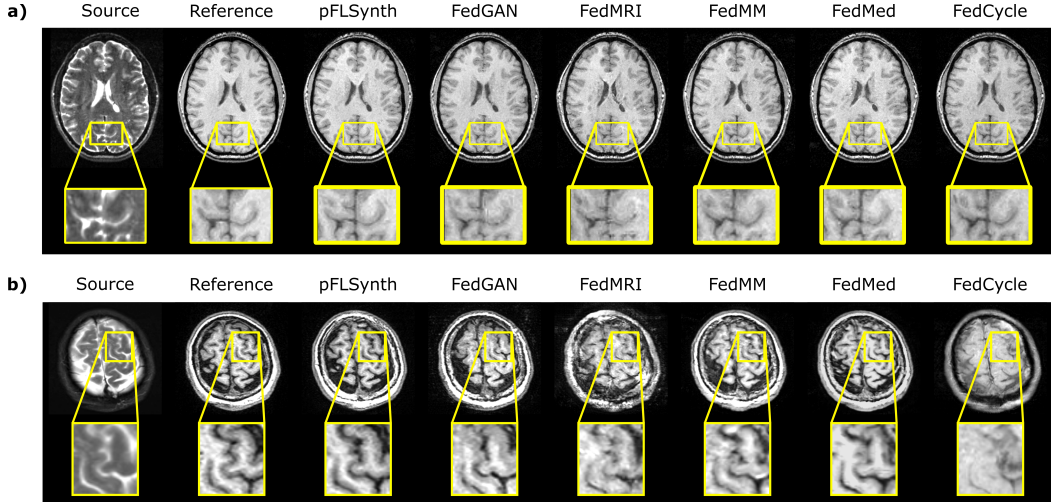


Figure 4: Federated synthesis under a task configuration variable within sites ($T_1 \rightarrow T_2$ and $T_2 \rightarrow T_1$), albeit common across sites. Source, reference target, and synthetic target images from competing methods are shown. Representative images are shown from a) MIDAS, b) OASIS. Overall, pFLSynth synthesizes images with fewer artifacts and lower noise levels compared to other federated methods.

for OASIS, where FedMRI yields lower FID in $T_1 \rightarrow T_2$. Importantly, pFLSynth outperforms the central benchmark in all tasks ($p < 0.05$), except for MIDAS and OASIS, where the benchmark yields moderately lower FID in a single task. On average across tasks and sites, pFLSynth achieves 2.0dB higher PSNR, 5.0% higher SSIM, and 24.9 lower FID over competing federated baselines. Note that pFLSynth offers higher benefits over competing methods in this variable task configuration compared to the less stringent configurations, suggesting the importance of the personalization elements in

		IXI		BRATS		MIDAS		OASIS	
		$T_1 \rightarrow T_2$	$T_2 \rightarrow T_1$						
Central	P \uparrow	28.2 \pm 1.2	27.8 \pm 1.1	26.0 \pm 0.8	24.4 \pm 1.8	27.9 \pm 0.6	26.1 \pm 1.2	25.0 \pm 0.5	21.3 \pm 0.8
	S \uparrow	93.9 \pm 1.4	94.4 \pm 1.1	92.9 \pm 1.0	92.4 \pm 1.0	91.5 \pm 1.0	86.9 \pm 2.2	83.2 \pm 2.4	76.9 \pm 2.0
	F \downarrow	8.6	28.5	27.5	13.6	10.4	11.8	22.8	20.1
pFLSynth	P \uparrow	28.1\pm1.2	27.7\pm1.1	26.0\pm0.9	24.8\pm1.7	28.1\pm0.6	26.2 \pm 1.1	24.9\pm0.8	21.3\pm0.7
	S \uparrow	93.8\pm1.3	94.4\pm1.3	92.9\pm1.0	92.5\pm1.0	91.9\pm0.9	86.6\pm2.1	83.6\pm2.5	76.0\pm2.9
	F \downarrow	8.7	28.2	26.9	13.8	9.5	10.7	34.6	21.8
FedGAN	P \uparrow	26.9 \pm 1.0	26.5 \pm 0.8	25.6 \pm 0.8	24.3 \pm 1.9	27.4 \pm 0.5	25.5 \pm 1.0	24.2 \pm 0.5	20.6 \pm 0.7
	S \uparrow	92.3 \pm 1.5	92.9 \pm 1.4	92.4 \pm 1.0	92.3 \pm 1.0	91.2 \pm 1.0	85.7 \pm 1.9	81.2 \pm 1.9	75.3 \pm 2.9
	F \downarrow	12.9	32.1	23.1	11.9	10.6	11.6	43.1	45.8
FedMRI	P \uparrow	27.0 \pm 1.0	26.7 \pm 1.0	25.4 \pm 0.9	24.2 \pm 1.5	27.1 \pm 0.5	25.4 \pm 1.0	22.6 \pm 0.5	19.4 \pm 0.6
	S \uparrow	92.9 \pm 1.4	93.5 \pm 1.3	92.2 \pm 1.1	91.6 \pm 1.0	90.2 \pm 1.2	85.3 \pm 1.9	73.4 \pm 2.1	68.2 \pm 2.6
	F \downarrow	13.6	35.2	35.3	16.6	13.2	18.5	80.6	55.7
FedMM	P \uparrow	26.4 \pm 1.1	26.6 \pm 1.0	25.4 \pm 0.7	24.3 \pm 1.7	27.5 \pm 0.5	25.6 \pm 1.1	23.6 \pm 0.5	20.5 \pm 0.6
	S \uparrow	91.5 \pm 1.8	92.7 \pm 1.3	92.3 \pm 1.0	91.2 \pm 1.0	90.7 \pm 0.9	86.1 \pm 1.9	78.3 \pm 2.6	73.7 \pm 3.0
	F \downarrow	20.4	39.2	32.3	13.7	10.5	12.3	45.1	30.3
FedMed	P \uparrow	26.6 \pm 1.1	26.5 \pm 1.1	25.3 \pm 0.8	24.2 \pm 1.6	27.3 \pm 0.5	25.5 \pm 1.1	23.6 \pm 0.6	20.5 \pm 0.6
	S \uparrow	92.2 \pm 1.7	93.1 \pm 1.3	92.2 \pm 0.9	91.9 \pm 0.9	90.6 \pm 1.0	85.8 \pm 1.8	76.6 \pm 2.5	74.1 \pm 2.9
	F \downarrow	14.3	38.4	29.5	14.8	10.3	12.1	56.4	31.2
FedCycle	P \uparrow	26.9 \pm 1.0	26.5 \pm 1.0	25.5 \pm 0.8	24.4 \pm 1.7	27.5 \pm 0.5	27.7\pm1.2	23.3 \pm 0.7	20.6 \pm 0.8
	S \uparrow	92.7 \pm 1.3	93.3 \pm 1.3	92.5 \pm 1.0	92.2 \pm 1.0	91.0 \pm 1.0	86.3 \pm 2.1	76.6\pm2.5	74.6 \pm 3.0
	F \downarrow	13.4	33.9	29.4	13.7	10.1	11.6	51.6	33.3

Table 2: PSNR (P, dB), SSIM (S, %), and FID (F) performance in a variable set of synthesis tasks within sites (i.e., $T_1 \rightarrow T_2$ and $T_2 \rightarrow T_1$).

maintaining reliable synthesis performance. Representative target images synthesized by competing methods are displayed in Fig. 5. Similar to other configurations, pFLSynth generates images with reduced artifacts and noise, more accurately depicting pathological tissue. Taken together, these findings corroborate the robustness of pFLSynth against implicit and explicit data heterogeneity in multi-contrast MRI synthesis.

5.4 Complexity and communication load

A practical concern for network models adopted for federated learning is their efficiency in decentralized settings. We thus examined the practicality of the network architectures used in competing methods. Run times, memory usage, model complexity, and communication load were measured. Table 4 lists the inference time per cross-section, video memory utilization, number of model parameters including both shared and unshared subnetworks, and number of parameters communicated between sites and the server. Although pFLSynth has the highest model complexity, it has comparable memory utilization to other methods. While its run time is notably longer than federated methods based on UNet backbones, it maintains a short processing time on an absolute scale, suggesting that it can be efficiently trained in individual sites. Note that, despite its overall complexity, pFLSynth leverages partial network aggregation where upstream layers of the generator are not communicated. It is among the top two methods in terms of communication efficiency, showcasing a secondary benefit of partial network aggregation in pFLSynth.

		IXI		BRATS		MIDAS		OASIS	
		$T_1 \rightarrow T_2$	$T_2 \rightarrow PD$	$T_1 \rightarrow T_2$	$FR \rightarrow T_2$	$T_1 \rightarrow T_2$	$T_2 \rightarrow T_1$	$T_1 \rightarrow T_2$	$T_2 \rightarrow FR$
Central	P \uparrow	25.2 \pm 1.3	26.8 \pm 1.8	24.5 \pm 1.0	21.8 \pm 1.5	22.7 \pm 1.0	20.8 \pm 1.0	24.3 \pm 1.2	21.9 \pm 1.4
	S \uparrow	89.6 \pm 2.9	86.6 \pm 6.4	90.4 \pm 1.1	81.7 \pm 5.1	70.2 \pm 6.7	67.1 \pm 2.7	81.6 \pm 3.6	79.8 \pm 3.6
	F \downarrow	29.1	59.1	45.3	85.1	48.0	11.5	39.1	26.4
pFLSynth	P \uparrow	27.9\pm1.2	31.2\pm1.0	25.6\pm1.0	23.4\pm1.0	25.9\pm0.6	25.1 \pm 1.1	23.4\pm1.8	21.1\pm1.9
	S \uparrow	93.7\pm1.5	97.2\pm0.5	92.4\pm1.2	88.8\pm1.8	89.0\pm1.2	84.1 \pm 2.1	81.7\pm3.3	76.4\pm5.2
	F \downarrow	8.6	22.1	23.2	42.6	10.4	12.4	46.7	29.7
FedGAN	P \uparrow	26.8 \pm 1.1	29.7 \pm 0.9	23.9 \pm 1.1	20.1 \pm 1.5	20.7 \pm 0.9	25.4 \pm 1.0	22.0 \pm 1.6	19.9 \pm 1.8
	S \uparrow	92.2 \pm 1.7	96.2 \pm 0.6	89.9 \pm 1.5	81.5 \pm 2.7	76.4 \pm 3.2	85.5\pm2.1	78.2 \pm 3.3	75.2 \pm 5.5
	F \downarrow	14.4	26.0	42.4	107.0	117.2	14.3	47.7	40.1
FedMRI	P \uparrow	27.0 \pm 1.1	30.7 \pm 0.9	23.7 \pm 1.1	22.7 \pm 0.9	24.9 \pm 0.5	23.1 \pm 0.9	21.8 \pm 1.3	20.0 \pm 1.5
	S \uparrow	92.7 \pm 1.5	96.6 \pm 0.5	89.8 \pm 1.7	87.8 \pm 1.6	86.7 \pm 1.2	79.0 \pm 2.2	77.7 \pm 2.7	72.3 \pm 5.0
	F \downarrow	12.6	26.0	43.4	56.6	21.6	33.8	40.4	38.0
FedMM	P \uparrow	27.1 \pm 1.0	30.3 \pm 0.8	24.2 \pm 0.8	22.9 \pm 0.9	17.5 \pm 0.8	24.0 \pm 1.4	21.7 \pm 1.3	19.2 \pm 1.3
	S \uparrow	92.7 \pm 1.6	96.5 \pm 0.5	90.5 \pm 1.1	87.9 \pm 1.8	62.5 \pm 3.2	80.8 \pm 2.5	72.6 \pm 4.2	68.8 \pm 6.2
	F \downarrow	13.4	24.8	36.4	46.6	169.6	26.9	45.4	39.7
FedMed	P \uparrow	26.2 \pm 0.9	28.7 \pm 0.8	22.8 \pm 1.1	20.1 \pm 1.0	25.5 \pm 0.7	24.0 \pm 1.4	21.4 \pm 1.2	19.6 \pm 1.8
	S \uparrow	91.5 \pm 1.6	95.1 \pm 0.7	88.2 \pm 1.6	82.3 \pm 2.0	88.9 \pm 1.2	80.8 \pm 2.5	75.7 \pm 3.3	71.2 \pm 5.3
	F \downarrow	18.8	29.4	59.9	121.4	19.9	17.3	53.9	39.9
FedCycle	P \uparrow	26.8 \pm 1.0	28.7 \pm 0.8	23.5 \pm 0.9	18.9 \pm 1.0	17.3 \pm 0.9	25.5\pm1.0	21.6 \pm 1.3	19.7 \pm 1.4
	S \uparrow	92.5 \pm 1.5	95.6 \pm 0.7	89.3 \pm 1.0	80.1 \pm 2.7	62.0 \pm 3.2	84.0 \pm 2.2	65.7 \pm 5.1	64.0 \pm 8.4
	F \downarrow	16.5	31.0	56.1	139.1	176.8	14.0	49.8	47.9

Table 3: PSNR (P, dB), SSIM (S, %), and FID (F) performance in a variable set of synthesis tasks both within and across sites. FR denotes FLAIR.

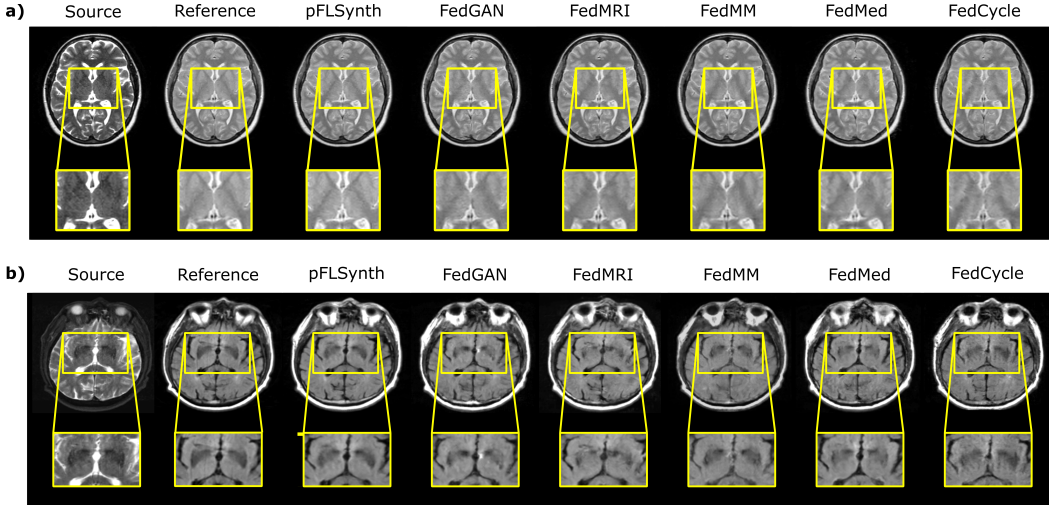


Figure 5: Federated synthesis under a task configuration variable within and across sites ($T_2 \rightarrow T_1$ and $T_2 \rightarrow PD$ in IXI, $T_2 \rightarrow T_1$ and $FR \rightarrow T_2$ in BRATS, $T_1 \rightarrow T_2$ and $T_2 \rightarrow T_1$ in MIDAS, $T_2 \rightarrow T_1$ and $T_2 \rightarrow FR$ in OASIS). Source, reference target, and synthetic target images from competing methods are shown. Representative images are shown from a) $T_2 \rightarrow PD$ in IXI, b) $T_2 \rightarrow FR$ in OASIS. Overall, pFLSynth synthesizes images with fewer artifacts and lower noise levels compared to other federated methods.

6 Discussion

Federated MRI synthesis involves multi-site imaging data collected under distinct settings, so it has to operate under distributional heterogeneity [21]. A recent study has considered FedAvg optimization of cycle-consistent GAN models to enable decentralized training of MRI synthesis [49]. However, no prior study has proposed a dedicated mechanism to mitigate the undesirable influences of data heterogeneity on FL-trained synthesis models beyond the level inherently offered by vanilla federated averaging. Therefore, pFLSynth is the first FL method to personalize a global synthesis model to each individual site and synthesis task. Experiments on multi-site brain MRI data demonstrate that pFLSynth offers on par performance to a centralized benchmark while outperforming alternative federated baselines. Our results suggest that pFLSynth can improve generalizability and flexibility in multi-site collaborations by permitting training on imaging data from diverse sources and protocols. Among key concerns for modeling in the FL framework are the computation and communication costs

	Central	pFLSynth	FedGAN	FedMRI	FedMM	FedMed	FedCycle
Inference (ms)	12.48	14.10	12.48	5.13	5.53	5.13	7.44
Memory (GB)	1.67	1.73	1.67	1.63	1.63	1.63	1.65
Complexity (M)	14.27	18.75	14.27	10.51	10.52	10.51	12.75
Communication (M)	-	6.52	11.51	4.71	7.77	7.77	9.99

Table 4: Inference time (milliseconds), memory usage (gigabytes of VRAM), local model complexity (millions of parameters), and communication load (millions of parameters) for competing methods.

associated with network architectures. The competing methods for FL-based synthesis in this study were all based on adversarial architectures with a globally-shared generator and local discriminators [55]. As the generator typically dominates the overall complexity of GAN models, model training and transfer costs are primarily determined by its structure. Note that FedCycle and pFLSynth both use relatively compact network blocks to create latent variables that marginally limit these benefits. Yet, the networks that exercise partial network sharing, pFLSynth and FedMRI, further alleviate communication costs. Overall, pFLSynth performs competitively against baselines regarding both computation and communication costs.

The FL framework communicates parameters of locally-trained models as opposed to explicit transfer of imaging data in order to mitigate patient privacy risks. Yet, patients privacy still remains an important concern for FL as membership inference attacks might leak information about training data from model parameters [8]. Here, we considered an FL setup where only generators of adversarial models were shared across sites, but the discriminators were never communicated. This procedure has been reported to be relatively resilient against inference attacks in recent reports [70]. Nevertheless, the risk for potential information leaks can be further minimized by adopting differentially private training procedures [49, 71], or by extending the size and diversity of the training datasets to implicitly improve differential privacy between training and synthetic samples as would be produced by a trained GAN model [72]. Future studies are warranted to systematically examine the privacy properties of various FL-based synthesis methods in multi-contrast MRI.

The proposed approach is open to further development along several technical lines. Here, we considered training of MRI synthesis models on paired datasets with spatially registered source and target images from a matching set of subjects [7]. Utilization of unpaired data can facilitate compilation of broader datasets that may be desired when training substantially complex models. In those cases, cycle-consistent [73, 74] or semi-supervised training [75, 76] strategies can be adopted. Performance during unpaired training might further be enhanced via dedicated spatial alignment modules [77]. Here, we considered one-to-one synthesis tasks where both source and target images

were from a single contrast. When tissue information required to synthesize the target modality is not sufficiently evident in a single source modality, pFLSynth can be generalized to perform many-to-one mapping by incorporating additional sources as separate input channels [41, 43, 68]. Recent studies have reported benefits for training centralized models based on transformer architectures as opposed to traditional CNNs in medical imaging tasks [78, 46]. Synthesis performance for pFLSynth might also benefit from adoption of transformer-based generators augmented with latent variables [79]. That said, relatively light transformer modules might be preferable to maintain reasonable computation and communication costs in the FL setup. The proposed method can also be adopted for other dense-prediction tasks in medical imaging such as MRI reconstruction or super-resolution. In these applications, personalization with site- and contrast-specific latents can similarly permit federated training of a unified model that can reliably handle data for multiple distinct MRI contrasts, to reduce the need for training separate models for each contrast.

7 Conclusion

Here, we introduced a novel method for multi-contrast MRI synthesis based on federated learning (FL) of an adversarial model equipped with personalization blocks and partial network aggregation. Benefits over state-of-the-art federated methods were demonstrated for brain image synthesis considering different public datasets and source-target configurations. Improved generalization against implicit and explicit domain shifts renders pFLSynth a promising candidate for multi-site collaborations in MRI contrast translation. pFLSynth might also be used for other medical image translation tasks involving modalities such as CT or PET.

References

- [1] S. Bakas, A. Sotiras, M. Bilello, M. Rozycki, J. Kirby, J. Freymann, K. Farahani, and C. Davatzikos, “Advancing the cancer genome atlas glioma MRI collections with expert segmentation labels and radiomic features,” *Sci. Data*, vol. 4, 2017.
- [2] K. Krupa and M. Bekiesińska-Figatowska, “Artifacts in magnetic resonance imaging,” *Pol. J. Radiol.*, vol. 80, pp. 93–106, 2015.
- [3] J. E. Iglesias, E. Konukoglu, D. Zikic, B. Glocker, K. Van Leemput, and B. Fischl, “Is synthesizing MRI contrast useful for inter-modality analysis?” in *Med. Image Comput. Comput. Assist. Interv.*, 2013, pp. 631–638.
- [4] V. Sevetlidis, M. V. Giuffrida, and S. A. Tsaftaris, “Whole image synthesis using a deep encoder-decoder network,” in *Simul. Synth. Med. Imaging*, 2016, pp. 127–137.
- [5] T. Joyce, A. Chartsias, and S. A. Tsaftaris, “Robust multi-modal MR image synthesis,” in *Med. Image Comput. Comput. Assist. Interv.*, 2017, pp. 347–355.
- [6] W. Wei, E. Poirion, B. Bodini, S. Durrleman, O. Colliot, B. Stankoff, and N. Ayache, “Fluid-attenuated inversion recovery MRI synthesis from multisequence MRI using three-dimensional fully convolutional networks for multiple sclerosis,” *J. Med. Imaging*, vol. 6, no. 1, p. 014005, 2019.
- [7] S. U. Dar, M. Yurt, L. Karacan, A. Erdem, E. Erdem, and T. Çukur, “Image synthesis in multi-contrast mri with conditional generative adversarial networks,” *IEEE Trans. Med. Imag.*, vol. 38, no. 10, pp. 2375–2388, 2019.
- [8] G. A. Kaassis, M. R. Makowski, D. Rueckert, and R. F. Braren, “Secure, privacy-preserving and federated machine learning in medical imaging,” *Nat. Mach. Intell.*, vol. 2, no. 6, pp. 305–311, 2020.

- [9] W. Li, F. Milletarì, D. Xu, N. Rieke, J. Hancox, W. Zhu, M. Baust, Y. Cheng, S. Ourselin, M. Cardoso, and A. Feng, “Privacy-preserving federated brain tumour segmentation,” in *Mach. Learn. Med. Imag.*, 2019, pp. 133–141.
- [10] M. J. Sheller, G. A. Reina, B. Edwards, J. Martin, and S. Bakas, “Multi-institutional deep learning modeling without sharing patient data: A feasibility study on brain tumor segmentation,” in *Med. Image Comput. Comput. Assist. Interv.*, 2019, pp. 92–104.
- [11] N. Rieke, J. Hancox, W. Li, F. Milletarì, H. R. Roth, S. Albarqouni, S. Bakas, M. N. Galtier, B. A. Landman, K. Maier-Hein, S. Ourselin, M. Sheller, R. M. Summers, A. Trask, D. Xu, M. Baust, and M. J. Cardoso, “The future of digital health with federated learning,” *npj Digital Medicine*, vol. 3, no. 1, p. 119, 2020.
- [12] H. R. Roth, K. Chang, P. Singh, N. Neumark, W. Li, V. Gupta, S. Gupta, L. Qu, A. Ihsani, B. C. Bizzo, and et al., “Federated Learning for Breast Density Classification: A Real-World Implementation,” in *DART, DCL*, 2020, p. 181–191.
- [13] X. Li, Y. Gu, N. Dvornek, L. H. Staib, P. Ventola, and J. S. Duncan, “Multi-site fmri analysis using privacy-preserving federated learning and domain adaptation: Abide results,” *Med. Image. Anal.*, vol. 65, p. 101765, 2020.
- [14] Q. Liu, C. Chen, J. Qin, Q. Dou, and P. Heng, “Feddg: Federated domain generalization on medical image segmentation via episodic learning in continuous frequency space,” in *Comput. Vis. Pattern Recognit.*, 2021, pp. 1013–1023.
- [15] H. B. McMahan, E. Moore, D. Ramage, S. Hampson, and B. A. y Arcas, “Communication-efficient learning of deep networks from decentralized data,” in *AISTATS*, 2017.
- [16] J. Wang, Z. Charles, Z. Xu, G. Joshi, H. B. McMahan, B. A. y Arcas, M. Al-Shedivat, G. Andrew, S. Avestimehr, K. Daly, D. Data, S. Diggavi, H. Eichner, A. Gadhikar, Z. Garrett, A. M. Girgis, F. Hanzely, A. Hard, C. He, S. Horvath, Z. Huo, A. Ingerman, M. Jaggi, T. Javidi, P. Kairouz, S. Kale, S. P. Karimireddy, J. Konecny, S. Koyejo, T. Li, L. Liu, M. Mohri, H. Qi, S. J. Reddi, P. Richtarik, K. Singhal, V. Smith, M. Soltanolkotabi, W. Song, A. T. Suresh, S. U. Stich, A. Talwalkar, H. Wang, B. Woodworth, S. Wu, F. X. Yu, H. Yuan, M. Zaheer, M. Zhang, T. Zhang, C. Zheng, C. Zhu, and W. Zhu, “A field guide to federated optimization,” *arXiv:2107.06917*, 2021.
- [17] T. Li, A. K. Sahu, A. S. Talwalkar, and V. Smith, “Federated learning: Challenges, methods, and future directions,” *IEEE Signal. Process. Mag.*, vol. 37, pp. 50–60, 2020.
- [18] N. Rieke, J. Hancox, W. Li, F. Milletari, H. Roth, S. Albarqouni, S. Bakas, M. Galtier, B. Landman, K. Maier-Hein, S. Ourselin, M. Sheller, R. Summers, A. Trask, D. Xu, M. Baust, and M. J. Cardoso, “The future of digital health with federated learning,” *npj Digital Medicine*, vol. 3, 12 2020.
- [19] M. Sheller, B. Edwards, G. Reina, J. Martin, S. Pati, A. Kotrotsou, M. Milchenko, W. Xu, D. Marcus, R. Colen, and S. Bakas, “Federated learning in medicine: facilitating multi-institutional collaborations without sharing patient data,” *Scientific Reports*, vol. 10, 07 2020.
- [20] H. R. Roth, D. Yang, W. Li, A. Myronenko, W. Zhu, Z. Xu, X. Wang, and D. Xu, “Federated whole prostate segmentation in MRI with personalized neural architectures,” in *Med. Image Comput. Comput. Assist. Interv.* Cham: Springer, 2021, pp. 357–366.
- [21] X. Li, M. Jiang, X. Zhang, M. Kamp, and Q. Dou, “FedBN: Federated learning on non-IID features via local batch normalization,” in *Int. Conf. Learn. Represent.*, 2021.
- [22] C. I. Bercea, B. Wiestler, D. Rueckert, and S. Albarqouni, “Feddis: Disentangled federated learning for unsupervised brain pathology segmentation,” *arXiv:2103.03705*, 2021.
- [23] S. Pati, U. Baid, M. Zenk, B. Edwards, M. Sheller, G. A. Reina, P. Foley, A. Gruzdev, J. Martin, S. Albarqouni, Y. Chen, R. T. Shinohara, A. Reinke, D. Zimmerer, J. B. Freymann, J. S. Kirby, C. Davatzikos, R. R. Colen, A. Kotrotsou, D. Marcus, M. Milchenko, A. Nazeri,

- H. Fathallah-Shaykh, R. Wiest, A. Jakab, M.-A. Weber, A. Mahajan, L. Maier-Hein, J. Kleesiek, B. Menze, K. Maier-Hein, and S. Bakas, “The federated tumor segmentation (fets) challenge,” *arXiv:2105.05874*, 2021.
- [24] D. Yang, Z. Xu, W. Li, A. Myronenko, H. R. Roth, S. Harmon, S. Xu, B. Turkbey, E. Turkbey, X. Wang, W. Zhu, G. Carrafiello, F. Patella, M. Cariati, H. Obinata, H. Mori, K. Tamura, P. An, B. J. Wood, and D. Xu, “Federated semi-supervised learning for COVID region segmentation in chest CT using multi-national data from China, Italy, Japan,” *Med. Image. Anal.*, vol. 70, p. 101992, 2021.
- [25] Z. Yan, J. Wicaksana, Z. Wang, X. Yang, and K.-T. Cheng, “Variation-aware federated learning with multi-source decentralized medical image data,” *IEEE J. Biomed. Health Inform.*, vol. 25, no. 7, pp. 2615–2628, 2021.
- [26] S. Park, G. Kim, J. Kim, B. Kim, and J. C. Ye, “Federated Split Task-Agnostic Vision Transformer for COVID-19 CXR Diagnosis,” in *Adv. Neural Inf. Process. Syst.*, 2021.
- [27] P. Guo, P. Wang, J. Zhou, S. Jiang, and V. M. Patel, “Multi-institutional Collaborations for Improving Deep Learning-based Magnetic Resonance Image Reconstruction Using Federated Learning,” *arXiv:2103.02148*, 2021.
- [28] C.-M. Feng, Y. Yan, H. Fu, Y. Xu, and L. Shao, “Specificity-Preserving Federated Learning for MR Image Reconstruction,” *arXiv:2112.05752*, 2021.
- [29] G. Elmas, S. U. Dar, Y. Korkmaz, E. Ceyani, B. Susam, M. Özbeý, S. Avestimehr, and T. Çukur, “Federated learning of generative image priors for MRI reconstruction,” *arXiv:2202.04175*, 2022.
- [30] R. Vemulapalli, H. Van Nguyen, and S. K. Zhou, “Unsupervised cross-modal synthesis of subject-specific scans,” in *Int. Conf. Comput. Vis.*, 2015, pp. 630–638.
- [31] A. Jog, A. Carass, S. Roy, D. L. Pham, and J. L. Prince, “Random forest regression for magnetic resonance image synthesis,” *Med. Image. Anal.*, vol. 35, pp. 475–488, 2017.
- [32] Y. Huang, L. Shao, and A. F. Frangi, “Cross-modality image synthesis via weakly coupled and geometry co-regularized joint dictionary learning,” *IEEE Trans. Med. Imag.*, vol. 37, no. 3, pp. 815–827, 2018.
- [33] C. Bowles, C. Qin, C. Ledig, R. Guerrero, R. Gunn, A. Hammers, E. Sakka, D. Dickie, M. Hernández, N. Royle, J. Wardlaw, H. Rhodius-Meester, B. Tijms, A. Lemstra, W. Flier, F. Barkhof, P. Scheltens, and D. Rueckert, “Pseudo-healthy image synthesis for white matter lesion segmentation,” in *Simul. Synth. Med. Imaging*, 2016, pp. 87–96.
- [34] A. Chartsias, T. Joyce, R. Dharmakumar, and S. A. Tsafaris, “Adversarial image synthesis for unpaired multi-modal cardiac data,” in *Simul. Synth. Med. Imaging*, 2017, pp. 3–13.
- [35] D. Nie, R. Trullo, J. Lian, L. Wang, C. Petitjean, S. Ruan, and Q. Wang, “Medical image synthesis with deep convolutional adversarial networks,” *IEEE Trans. Biomed. Eng.*, vol. 65, no. 12, pp. 2720–2730, 2018.
- [36] K. Armanious, C. Jiang, M. Fischer, T. Küstner, T. Hepp, K. Nikolaou, S. Gatidis, and B. Yang, “MedGAN: Medical image translation using GANs,” *Comput. Med. Imaging Graph.*, vol. 79, p. 101684, 2020.
- [37] B. Yu, L. Zhou, L. Wang, Y. Shi, J. Fripp, and P. Bourgeat, “Ea-GANs: Edge-Aware Generative Adversarial Networks for Cross-Modality MR Image Synthesis,” *IEEE Trans. Med. Imag.*, vol. 38, no. 7, pp. 1750–1762, 2019.
- [38] T. Zhou, H. Fu, G. Chen, J. Shen, and L. Shao, “Hi-Net: Hybrid-fusion network for multi-modal MR image synthesis,” *IEEE Trans. Med. Imag.*, vol. 39, no. 9, pp. 2772–2781, 2020.
- [39] Y. Luo, D. Nie, B. Zhan, Z. Li, X. Wu, J. Zhou, Y. Wang, and D. Shen, “Edge-preserving MRI image synthesis via adversarial network with iterative multi-scale fusion,” *Neurocomputing*, vol. 452, pp. 63–77, 2021.

- [40] B. Zhan, D. Li, Y. Wang, Z. Ma, X. Wu, J. Zhou, and L. Zhou, “LR-cGAN: Latent representation based conditional generative adversarial network for multi-modality MRI synthesis,” *Biomed. Signal Process. Control*, vol. 66, p. 102457, 2021.
- [41] M. Yurt, S. U. Dar, A. Erdem, E. Erdem, K. K. Oguz, and T. Çukur, “mustGAN: multi-stream generative adversarial networks for MR image synthesis,” *Med. Image. Anal.*, vol. 70, p. 101944, 2021.
- [42] A. Sharma and G. Hamarneh, “Missing MRI pulse sequence synthesis using multi-modal generative adversarial network,” *IEEE Trans. Med. Imag.*, vol. 39, no. 4, pp. 1170–1183, 2020.
- [43] D. Lee, J. Kim, W.-J. Moon, and J. C. Ye, “CollaGAN: Collaborative GAN for missing image data imputation,” in *Comput. Vis. Pattern Recognit.*, 2019, pp. 2487–2496.
- [44] H. Li, J. C. Paetzold, A. Sekuboyina, F. Kofler, J. Zhang, J. S. Kirschke, B. Wiestler, and B. Menze, “DiamondGAN: Unified multi-modal generative adversarial networks for MRI sequences synthesis,” in *Med. Image Comput. Comput. Assist. Interv.*, 2019, pp. 795–803.
- [45] G. Wang, E. Gong, S. Banerjee, D. Martin, E. Tong, J. Choi, H. Chen, M. Wintermark, J. M. Pauly, and G. Zaharchuk, “Synthesize high-quality multi-contrast magnetic resonance imaging from multi-echo acquisition using multi-task deep generative model,” *IEEE Trans. Med. Imag.*, vol. 39, no. 10, pp. 3089–3099, 2020.
- [46] O. Dalmaç, M. Yurt, and T. Çukur, “ResViT: Residual vision transformers for multi-modal medical image synthesis,” *IEEE Trans. Med. Imaging*, pp. 1–1, 2022. doi:10.1109/TMI.2022.3167808.
- [47] J. Song and J. C. Ye, “Federated cycleGAN for privacy-preserving image-to-image translation,” *arXiv:2106.09246*, 2021.
- [48] S. Che, Z. Kong, H. Peng, L. Sun, A. Leow, Y. Chen, and L. He, “Federated multi-view learning for private medical data integration and analysis,” *ACM Trans. Intell. Syst. Technol.*, vol. 13, no. 4, jun 2022. [Online]. Available: <https://doi.org/10.1145/3501816>
- [49] G. Xie, J. Wang, Y. Huang, Y. Li, Y. Zheng, F. Zheng, and Y. Jin, “FedMed-GAN: Federated domain translation on unsupervised cross-modality brain image synthesis,” *arXiv:2201.08953*, 2022.
- [50] X. Huang and S. Belongie, “Arbitrary style transfer in real-time with adaptive instance normalization,” in *ICCV*, 2017.
- [51] S. Khan, J. Huh, and J. C. Ye, “Switchable and tunable deep beamformer using adaptive instance normalization for medical ultrasound,” *IEEE Transactions on Medical Imaging*, vol. 41, no. 2, pp. 266–278, 2022.
- [52] J. Gu and J. C. Ye, “Adain-based tunable cyclegan for efficient unsupervised low-dose ct denoising,” *IEEE Transactions on Computational Imaging*, vol. PP, pp. 1–1, 01 2021.
- [53] H. Zhang, H. Li, J. Dillman, N. Parikh, and L. He, “Multi-contrast mri image synthesis using switchable cycle-consistent generative adversarial networks,” *Diagnostics*, vol. 12, p. 816, 03 2022.
- [54] J. Denck, J. Guehring, A. Maier, and E. Rothgang, “Mr-contrast-aware image-to-image translations with generative adversarial networks,” *International Journal of Computer Assisted Radiology and Surgery*, vol. 16, 06 2021.
- [55] M. Rasouli, T. Sun, and R. Rajagopal, “Fedgan: Federated generative adversarial networks for distributed data,” *arXiv:2006.07228*, 2020.
- [56] L. Zhang, B. Shen, A. Barnawi, S. Xi, N. Kumar, and Y. Wu, “FedDPGAN: Federated Differentially Private Generative Adversarial Networks Framework for the Detection of COVID-19 Pneumonia,” *Inf. Syst. Front.*, vol. 23, no. 6, pp. 1403–1415, 2021.

- [57] A. Beers, J. Brown, K. Chang, J. Campbell, S. Ostmo, M. Chiang, and J. Kalpathy-Cramer, “High-resolution medical image synthesis using progressively grown generative adversarial networks,” *arXiv:1805.03144*, 2018.
- [58] K. Armanious, C. Jiang, M. Fischer, T. Küstner, T. Hepp, K. Nikolaou, S. Gatidis, and B. Yang, “MedGAN: Medical image translation using GANs,” *Comput. Med. Imaging Grap.*, vol. 79, p. 101684, 2019.
- [59] K. He, X. Zhang, S. Ren, and J. Sun, “Deep residual learning for image recognition,” in *Comput. Vis. Pattern Recognit.*, 2016, pp. 770–778.
- [60] Y. Wang, W. Huang, F. Sun, T. Xu, Y. Rong, and J. Huang, “Deep multimodal fusion by channel exchanging,” in *Adv. Neural Inf. Process. Syst.*, 2020.
- [61] T. Karras, S. Laine, and T. Aila, “A style-based generator architecture for generative adversarial networks,” in *Comput. Vis. Pattern Recognit.*, 2019, pp. 4401–4410.
- [62] H. B. McMahan, E. Moore, D. Ramage, S. Hampson, and B. A. y. Arcas, “Communication-efficient learning of deep networks from decentralized data,” *arXiv:1602.05629*, 2016.
- [63] B. H. Menze *et al.*, “The multimodal brain tumor image segmentation benchmark (BRATS),” *IEEE Trans. Med. Imag.*, vol. 34, no. 10, pp. 1993–2024, 2015.
- [64] E. Bullitt, D. Zeng, G. Gerig, S. Aylward, S. Joshi, J. Smith, W. Lin, and M. Ewend, “Vessel tortuosity and brain tumor malignancy,” *Academic radiology*, vol. 12, pp. 1232–40, 11 2005.
- [65] P. J. LaMontagne, T. L. Benzinger, J. C. Morris, S. Keefe, R. Hornbeck, C. Xiong, E. Grant, J. Hassenstab, K. Moulder, A. G. Vlassenko, M. E. Raichle, C. Cruchaga, and D. Marcus, “Oasis-3: Longitudinal neuroimaging, clinical, and cognitive dataset for normal aging and alzheimer disease,” *medRxiv:2019.12.13.1901490*, 2019.
- [66] M. Jenkinson and S. Smith, “A global optimisation method for robust affine registration of brain images,” *Med. Image. Anal.*, vol. 5, pp. 143–156, 2001.
- [67] C.-M. Feng, Y. Yan, H. Fu, Y. Xu, and L. Shao, “Specificity-Preserving Federated Learning for MR Image Reconstruction,” *arXiv:2112.05752*, 2021.
- [68] A. Sharma and G. Hamarneh, “Missing MRI pulse sequence synthesis using multi-modal generative adversarial network,” *IEEE Trans. Med. Imag.*, vol. 39, pp. 1170–1183, 2020.
- [69] M. Heusel, H. Ramsauer, T. Unterthiner, B. Nessler, and S. Hochreiter, “GANs trained by a two time-scale update rule converge to a local nash equilibrium,” in *Adv Neural Inf Process Syst*, 2017, p. 6629–6640.
- [70] T. Han, S. Nebelung, C. Haarburger, N. Horst, S. Reinartz, D. Merhof, F. Kiessling, V. Schulz, and D. Truhn, “Breaking medical data sharing boundaries by using synthesized radiographs,” *Sci Adv*, vol. 6, no. 49, p. eabb7973, 2020.
- [71] A. Ziller, D. Usynin, M. Knolle, K. Hammerl, D. Rueckert, and G. Kaassis, “Complex-valued deep learning with differential privacy,” *arXiv:2110.03478*, 2021.
- [72] Q. Feng, C. Guo, F. Benitez-Quiroz, and A. Martinez, “When do GANs replicate? on the choice of dataset size,” in *Int. Conf. Comput. Vis.*, 2021, pp. 6701–6710.
- [73] J. Wolterink, A. M. Dinkla, M. Savenije, P. Seevinck, C. Berg, and I. Isgum, “Deep MR to CT synthesis using unpaired data,” in *Simul. Synth. Med. Imaging*, 2017, pp. 14–23.
- [74] Y. Ge, D. Wei, Z. Xue, Q. Wang, X. Zhou, Y. Zhan, and S. Liao, “Unpaired MR to CT synthesis with explicit structural constrained adversarial learning,” in *Int. Symp. Biomed. Imaging*, 2019, pp. 1096–1099.
- [75] C.-B. Jin, H. Kim, M. Liu, W. Jung, S. Joo, E. Park, Y. S. Ahn, I. H. Han, J. I. Lee, and X. Cui, “Deep CT to MR synthesis using paired and unpaired data,” *Sensors*, vol. 19, no. 10, p. 2361, 2019.

- [76] M. Yurt, S. U. H. Dar, M. Özbey, B. Tinaz, K. K. Oğuz, and T. Çukur, “Semi-supervised learning of mutually accelerated MRI synthesis without fully-sampled ground truths,” *arXiv:2011.14347*, 2021.
- [77] G. Xie, J. Wang, Y. Huang, Y. Zheng, F. Zheng, and Y. Jin, “Fedmed-atl: Misaligned unpaired brain image synthesis via affine transform loss,” *arXiv:2201.12589*, 2022.
- [78] A. Güngör, B. Askin, D. A. Soydan, E. U. Saritas, C. B. Top, and T. Çukur, “TranSMS: Transformers for Super-Resolution Calibration in Magnetic Particle Imaging,” *arXiv:2111.02163*, 2021.
- [79] Y. Korkmaz, S. U. Dar, M. Yurt, M. Özbey, and T. Çukur, “Unsupervised mri reconstruction via zero-shot learned adversarial transformers,” *IEEE Trans. Med. Imag.*, vol. 41, no. 7, pp. 1747–1763, 2022.